ADVANCED MATERIALS
www.advmat.de

A Library of Atomically Thin 2D Materials Featuring the Conductive-Point Resistive Switching Phenomenon

*Ruijing Ge, Xiaohan Wu, Liangbo Liang, Saban M. Hus, Yuqian Gu, Emmanuel Okogbue, Harry Chou, Jianping Shi, Yanfeng Zhang, Sanjay K. Banerjee, Yeonwoong Jung, Jack C. Lee, and Deji Akinwande**

Non-volatile resistive switching (NVRS) is a widely available effect in transitional metal oxides, colloquially known as memristors, and of broad interest for memory technology and neuromorphic computing. Until recently, NVRS was not known in other transitional metal dichalcogenides (TMDs), an important material class owing to their atomic thinness enabling the ultimate dimensional scaling. Here, various monolayer or few-layer 2D materials are presented in the conventional vertical structure that exhibit NVRS, including TMDs (MX_2, M = transitional metal, e.g., Mo, W, Re, Sn, or Pt; X = chalcogen, e.g., S, Se, or Te), TMD heterostructure (WS_2/MoS_2), and an atomically thin insulator (h-BN). These results indicate the universality of the phenomenon in 2D non-conductive materials, and feature low switching voltage, large ON/OFF ratio, and forming-free characteristic. A dissociation–diffusion–adsorption model is proposed, attributing the enhanced conductance to metal atoms/ions adsorption into intrinsic vacancies, a conductive-point mechanism supported by first-principle calculations and scanning tunneling microscopy characterizations. The results motivate further research in the understanding and applications of defects in 2D materials.

2D materials have attracted much attention in the last decade due to their remarkable electronic, optical, mechanical, and thermal properties.[1–3] After graphene was systematically identified and elucidated in 2004, more and more 2D materials have been re-discovered and investigated, including transition metal dichalcogenides (TMDs) and hexagonal boron nitride (h-BN).[1] Now the collection of 2D materials has expanded to several hundred with diverse properties in terms of their composition, bandgap, mobility, strain limit, etc.[4] The semiconductor industry can considerably benefit from the broad platform provided by the portfolio of 2D materials to advance electron devices, especially memory devices that is currently the technology driver.

In this context, non-volatile resistive switching (NVRS) device, also known colloquially as memristor[5] or atomristor[6] in atomically thin material, is an emerging memory device where the device resistance can be modulated between a high resistance state (HRS) and a low resistance state (LRS) via an electrical field. This phenomenon has been observed in various multilayer 2D materials, including graphene oxide,[7] functionalized or partly oxidized TMDs,[8,9] and degraded black phosphorus (BP).[10] In 2015, monolayer MoS_2 was shown to feature NVRS in a lateral device structure.[11] Though lateral structures can offer an additional terminal for field-effect control, they, unfortunately lack the integration density achievable with two-terminal vertical memory devices. Moreover, the gap between two lateral electrodes flanking the MoS_2 flake has been on the order of micrometer and thus a high switching voltage (≈20–100 V) was needed. In contrast, it is the conventional thinking in

Dr. R. Ge, X. Wu, Dr. S. M. Hus, Y. Gu, Dr. H. Chou, Prof. S. K. Banerjee, Prof. J. C. Lee, Prof. D. Akinwande
Microelectronics Research Center
The University of Texas at Austin
Austin, TX 78758, USA
E-mail: deji@ece.utexas.edu

Dr. L. Liang
Center for Nanophase Materials Sciences
Oak Ridge National Laboratory
Oak Ridge, TN 37831, USA

E. Okogbue, Prof. Y. Jung
Nanoscience Technology Center
and Department of Electrical Engineering
University of Central Florida
Orlando, FL 32826, USA

Dr. J. Shi, Prof. Y. Zhang
Department of Materials Science and Engineering
College of Engineering
Peking University
Beijing 100871, China

Dr. J. Shi
The Institute for Advanced Studies
Wuhan University
Wuhan 430072, China

Prof. Y. Jung
Department of Materials Science and Technology
University of Central Florida
Orlando, FL 32816, USA

The ORCID identification number(s) for the author(s) of this article can be found under https://doi.org/10.1002/adma.202007792.

DOI: 10.1002/adma.202007792

metal oxides that resistance switching cannot scale below a few nanometers because of excessive leakage.[5,12] Owing to the similar consideration of tunneling or leakage currents that may pass through the atomically thin barrier, monolayer 2D materials were not expected to exhibit NVRS in the industrially popular metal/active material/metal vertical structure. Even in recent publications about novel 2D materials based vertical structure memristors, most of the reports have been on multilayer[13] or even thick materials.[14] Fortunately, that contemporary view was overturned by our first demonstration of NVRS in monolayer MoS_2 and h-BN sandwiched between two metal electrodes, substantially reducing the interelectrode distance to sub-nanometers, and resulting in the thinnest memory cells with smaller switching voltages (0.5–3 V) and higher density prospects.[6,15,16] In this paper, we expand the collection of 2D atomic sheets showing NVRS to a dozen materials, indicating its potential universality in ultrathin non-metallic 2D materials. Moreover, we propose the dissociation–diffusion–adsorption (DDA) model to describe the common mechanism behind bipolar NVRS in 2D crystalline monolayers, a model supported by density functional theory (DFT) calculations showing favorable adsorption of metal atom/ion into native defects (e.g., sulfur vacancy in MoS_2). Our work elucidates a broad library consisting of various 2D atomic sheets with different electronic, thermal, and mechanical properties for applications including high-density memory, neuromorphic computing, flexible nanoelectronics, and radio-frequency (RF) switches.[6,17–19]

In this work, a dozen 2D materials were investigated for nonvolatile resistive switching, including transition metal sulfides (MS_2, M = Mo, W, Re, Sn), transition metal selenides (MSe_2, M = Mo, W, Re, Sn, Pt), a transition metal telluride ($MoTe_2$), a TMD heterostructure (WS_2/MoS_2), and an insulator (h-BN), as shown in **Figure 1**a–c. Transition metal sulfides, selenides, and tellurides are the most common 2D TMDs to date. Here, we purposely pick these representative 2D TMDs, and h-BN corresponding to semiconductor and insulator materials, respectively.[1] These selected 2D materials can be readily grown as mono or few layers with unambiguous characterization of material quality and thickness. More 2D films are expected to be added to this library as material synthesis and transfer progresses. In addition, the van der Waals interlayer interaction enables the possibility to reassemble different 2D materials into vertically stacked heterostructure,[20] and resistive switching in a representative WS_2/MoS_2 heterostructure is also demonstrated in this work. All different atomically thin 2D materials and their combination provide various building blocks with unique electrical, thermal, and optical properties for a large range of memory applications.[20] Crossbar devices (Figure 1d,e) were mainly employed to investigate the NVRS behavior with the stacking of Au (bottom electrode, BE)/2D material (active layer)/Au (top electrode, TE).[21] Au was initially chosen as a noble metal electrode to rule out potential memory effect from interfacial metallic oxides.[6] Subsequently, other common metals such as Cu, Ni, Ag, 1L graphene (at interface, device structure from top to bottom Au/1L graphene/MoS_2/Au/SiO_2/Si)[6] have also been successful electrodes for observing the intrinsic NVRS in 2D materials.[6,15,19] The bottom electrodes were prepared on Si/SiO_2 substrate and then a specific 2D material was subsequently transferred onto it, followed by the top electrode lithography and deposition. The device area, defined by the overlapped region between BE and TE, can be down to 0.1×0.1 um^2.

All the 2D materials investigated here were obtained from collaborators or commercial vendors.[22–25] The majority of the 2D materials in this work are monolayer films except for few-layer SnS_2, $SnSe_2$, $PtSe_2$, and $MoTe_2$ owing to the difficulty in acquiring high-quality and air-stable monolayer counterparts. Raman spectroscopy (**Figure 2**) were performed to verify the layer thickness, crystal quality, and phases. As an example TMD material, MoS_2 has two characteristic peaks, corresponding to

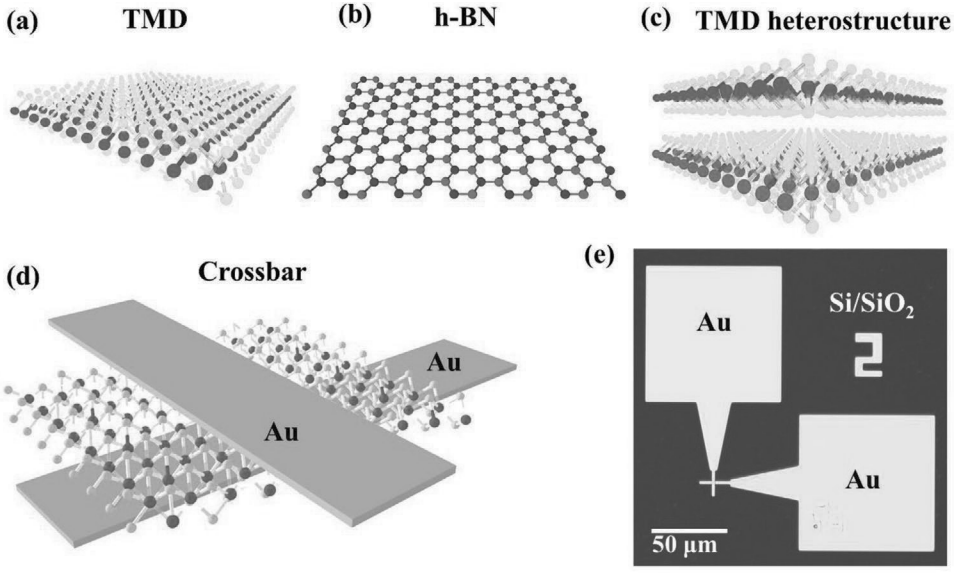

Figure 1. Materials and device structures. a–c) Schematics for diverse 2D atomic sheets used as the active layer in memristors, including: a) TMD, b) h-BN, and c) TMD heterostructure. d) Schematic and e) optical image of metal–2D material–metal sandwich structure for crossbar devices, where 2D materials are functioning as the insulating barrier.

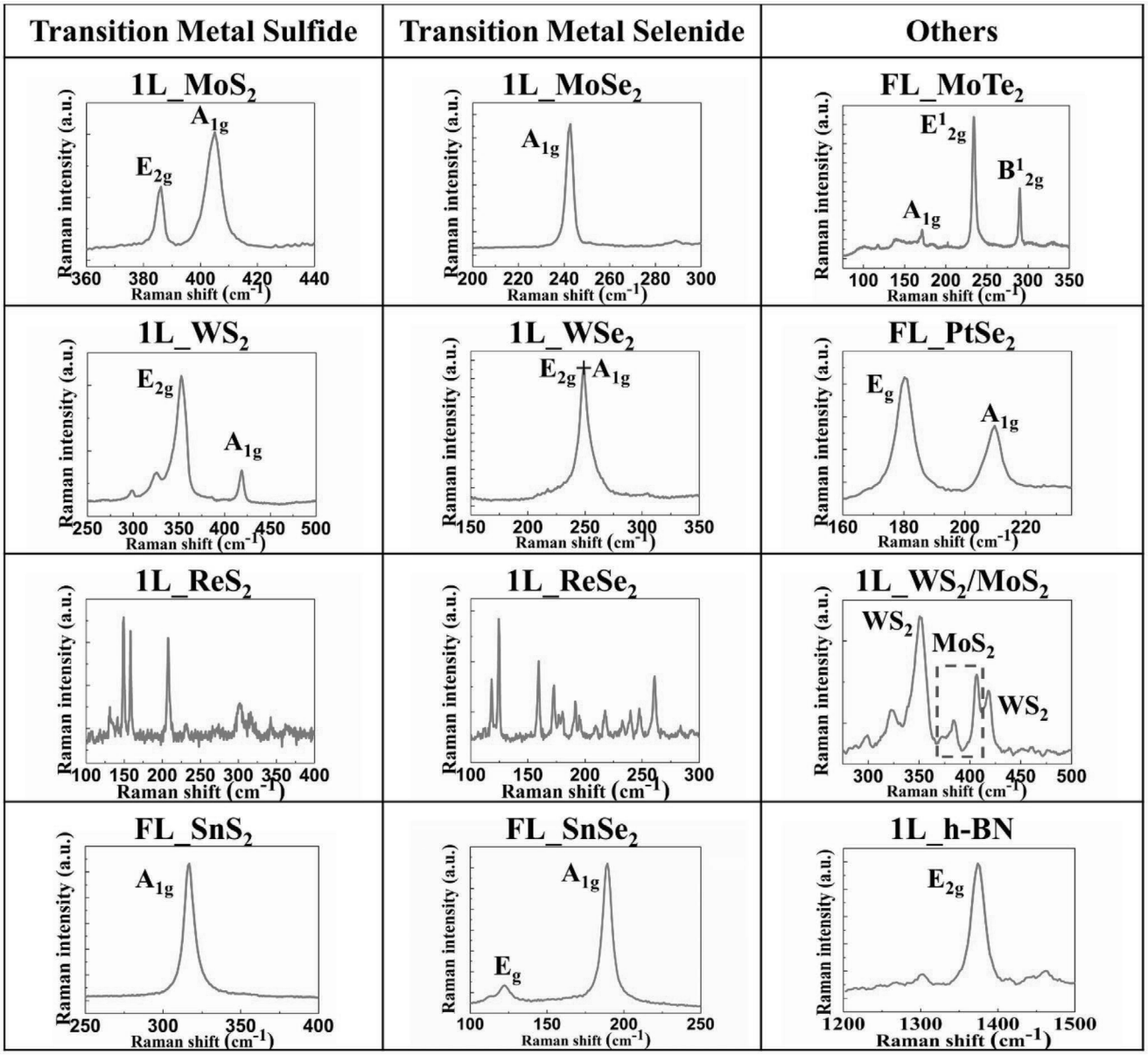

Figure 2. Raman spectra for various 2D materials used as the active layer. Raman spectra of monolayer (1L) MoS_2, WS_2, $MoSe_2$, WSe_2, h-BN, and few-layer (FL) $MoTe_2$ on Si/SiO_2 substrate, 1L ReS_2, $ReSe_2$ and FL SnS_2, $SnSe_2$ on sapphire substrate, 1L WS_2/MoS_2 heterostructure on Au foil, and FL $PtSe_2$ on Au film. Raman spectroscopy can be used to verify layer thickness, crystal quality, and phases of various 2D materials. A 532 nm laser was used for Raman studies.

the in-plane vibrational E_{2g} mode at 386 cm^{-1} and the out-of-plane vibrational A_{1g} mode at 405 cm^{-1}. The frequency difference (≈19 cm^{-1}) is in good agreement with that reported for monolayer characteristics of MoS_2.[26] Raman measurements performed among different locations on MoS_2 samples show nearly the same frequency difference between the two modes E_{2g} and A_{1g}, suggesting a uniform monolayer film. While the Raman spectrum of $MoTe_2$ can help identify the thickness as well as the phase. The modes observed in our $MoTe_2$ samples are A_{1g} (176 cm^{-1}), E^1_{2g} (236 cm^{-1}), and B^1_{2g} (290 cm^{-1}).[27] The B^1_{2g} mode, which originates from the interlayer interactions in the 2D limit, is a signature of few-layer $MoTe_2$, which is absent in monolayer or bulk samples. In addition, A_{1g} and E^1_{2g} modes are the fingerprint for 2H $MoTe_2$ in contrast to 1T′ $MoTe_2$.[28] All other Raman spectra are consistent with previous reports.[29–31] In addition, other characterizations using photoluminescence for MoS_2, $MoSe_2$, WS_2, and WSe_2, and atomic force microscopy (AFM) for $MoTe_2$ are shown in Figures S1 and S2, Supporting Information, indicating high quality and uniformity, and offer complimentary validation of film thickness.

In order to observe NVRS memory effect, DC electrical measurement was first performed on MoS_2-based memristors. **Figure 3** shows representative *I–V* switching curves for MoS_2, starting from the HRS, and featuring low currents in

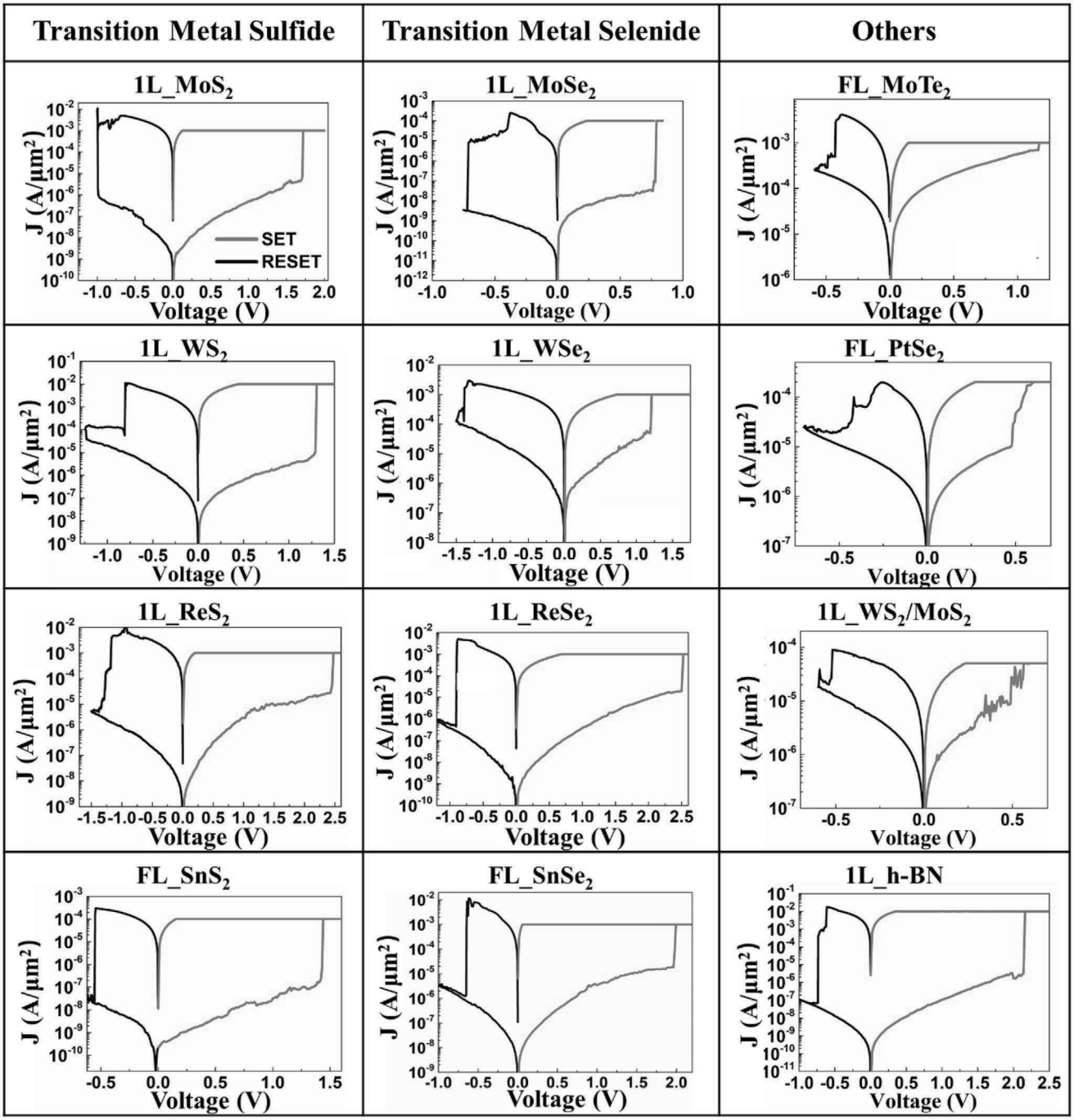

Figure 3. Representative *I*–*V* switching curves for various 2D materials. Typical *I*–*V* curves of resistive switching behavior in crossbar devices for 1L MoS_2, WS_2, ReS_2, $MoSe_2$, WSe_2, $ReSe_2$, h-BN, and FL SnS_2, $SnSe_2$, $MoTe_2$, and litho-free device for monolayer WS_2/MoS_2 heterostructure, and multilayer $PtSe_2$. The *y*-axes are normalized as current density *J*. The device areas are 1×1 μm^2 for MoS_2, WS_2, ReS_2, SnS_2, WSe_2, $ReSe_2$, $SnSe_2$, $MoTe_2$, and h-BN. 10×10 μm^2 device areas for $MoSe_2$ and $PtSe_2$, and 20×20 μm^2 for WS_2/MoS_2 heterostructure.

a fresh device. As the voltage sweeps to ≈1.75 V, the current abruptly increases to the compliance limit of 1 mA, which is commonly used to protect the device from hard breakdown.[5] This transition from HRS to LRS is the SET process. Afterward, the device remains in the LRS until a sufficient negative bias is applied. As the voltage sweeps to ≈–1 V, the device is switched back from LRS to HRS (the RESET process). Furthermore, to rule out any undesirable effect due to damage caused by e-beam deposition, we prepared devices with transferred top electrodes onto MoS_2[32] rather than direct deposition (Figure S3, Supporting Information). The devices with transferred TE also exhibit similar resistive switching behavior, indicating that the resistive switching is not originating from the damage by e-beam deposition.

Inspired by the switching phenomenon in MoS_2, we expanded to a larger collection of related materials in Figure 3. Interestingly, all the 2D materials investigated in our work exhibit resistive switching behavior with similar characteristics in switching voltage, ON/OFF ratio, RESET current, etc. The differences of switching performance among various 2D materials may be obscured behind cycle-to-cycle and device-to-device variations. For non-volatile resistive switching devices, variations are one of the major challenges due to the stochastic nature of the switching process.[33,34] Therefore, reducing variability for practical applications is an essential matter, which is expected to benefit from further advances in 2D material growth, device optimization, and testing protocol. Some mitigation strategies in material and interface engineering,[5,35] and programming optimization that can constrain the electrical variability[33] has proved to be effective for conventional transitional metal oxide memories. These techniques are necessary follow-up studies in order to develop 2D materials for practical memory benchmarking and applications.

Moreover, 2D materials offer multiple advantages in terms of switching performance including relatively low SET and RESET voltages, which are desirable in terms of power consumption. In addition, our devices do not require an electroforming process, which is necessary for most conventional transition metal oxide based memristors to create a soft-breakdown filament.[5] The ON/OFF ratio (the ratio of resistances at HRS and LRS) can reach up to 10^6 and multiple ON resistance states can be achieved under different compliance current,[6] highlighting its potential in multi-level memory cells and neuromorphic computing. Multiple references also support that 2D materials based memory devices have promising applications in neuromorphic computing.[13,19] Furthermore, our preliminary endurance test shows that $ReSe_2$ based memristor, as an example, can operate over 240 manual cycling in ambient atmosphere (Figure S4, Supporting Information). However, comprehensive reliability characteristics of 2D memory devices are still ongoing, and better performance can be expected after the optimization of material, fabrication, and testing protocol. As an example of material optimization, it was found that partial introduction of oxygen into multilayer MoS_2 substantially improved the endurance to over a million cycles.[36] A comparison with other emerging 2D NVRS devices has been included in Table S1, Supporting Information.

In order to elucidate the mechanism of non-volatile resistive switching in 2D monolayers, we propose a dissociation-diffusion-adsorption (DDA) model, illustrated in **Figure 4**a. In our device metrics, the symmetric electrodes choice (both TE and BE are gold in most cases) enables the formation of conductive point from either the top or bottom electrode.[12] The first step "dissociation" is based on the metal atom/ion dissociating from a cluster of metal atoms at the electrode–2D material interface. This process depends on the choice of metal electrode. Au electrodes, as a noble metal, were selected in this work to rule out any effect from interfacial metal oxidation to ensure that 2D materials play the essential role in the switching event. In addition, Au has relatively low atomization enthalpy (the amount of enthalpy change when a chemical substance's bonds are broken and the component atoms are reduced to individual atoms) among various transition metals and thus can serve as an appropriate electrode.[37] First-principle calculation results show that the dissociation energy required to move an Au atom sufficiently far from the bulk Au surface is 3.80 eV. This dissociation step is a common prerequisite for conventional conductive-bridge memory that relies on the formation of metal ions to create a conductive filament and has been investigated in previous reports,[38] so we will focus on the subsequent diffusion and adsorption steps.

After Au atom/ion dissociates from the electrode, it is either directly adsorbing (chemical bonding) into a vacancy when in close proximity (Case 1), or it first weakly bonds to the pristine region and then diffuses across the surface and finds a vacancy to fill and bond (Case 2). Both scenarios are illustrated schematically in Figure 4a. Case 1 is a simpler scenario including only two steps "dissociation" and "adsorption" courtesy of the initial close proximity to a vacancy. In contrast, Case 2 involves all 3 steps and is expected to be more common because the adsorbed neutral Au atom (Au) or positively charged Au ion (Au^{+1}) in the pristine region are energetically favorable compared to their isolated states as indicated by related calculations shown in Table S2, Supporting Information. Benefitting from the simplicity of Case 1, we are able to conduct first-principle calculations for all 12 materials investigated in this work. However, for the more probable Case 2, we focus on MoS_2 as a prototypical monolayer in the TMD family, owing to the system complexity.

For the simpler scenario of Case 1, the dissociated Au is in an isolated state and tends to directly get adsorbed into the defect, resulting in an atomic-scale conductive point that causes switching from a high-resistance state to a low-resistance state. The most common defects for 2D materials are believed to be vacancies, for example, S vacancy in MoS_2, Se vacancy in $MoSe_2$, B vacancy in BN, etc.[39,40] According to our first-principle calculations, there is no barrier energy for Au to move in and bind with the defect site, which is straightforward to understand since isolated Au is unstable and the system energy can decrease as Au moves toward a defect site. Figure 4b and Table S3, Supporting Information, shows the calculated adsorption energy of Au atom/ion into a vacancy site for various 2D materials. The negative adsorption energy (the energy difference between final state and initial state) indicates that adsorption is energetically preferable and releases energy, whereas a positive value means that the adsorption requires extra energy. Our calculations on diverse 2D materials suggest a common trend that both Au^{+1} and Au are energetically favorable to be adsorbed into defects, resulting in a SET process. To be more specific, Au^{+1} is the most favorable candidate, then neutral Au, and finally, negatively charged Au ion (Au^{-1}), which is the least energetically favorable for binding to the vacancy site. A primary reason for such a trend is that Au^{+1} is the most energetically unstable in an isolated vacuum state thus releasing the most energy when covalently binding to a vacancy site, followed by the neutral Au atom and then Au^{-1}.

With respect to the "diffusion" step in Case 2, Figure 4c shows the calculated diffusion pathway and barrier energies (the energy difference between transition state and initial state) of Au along MoS_2 surface from the top of one S atom to the top of a neighboring S atom in the pristine region away from

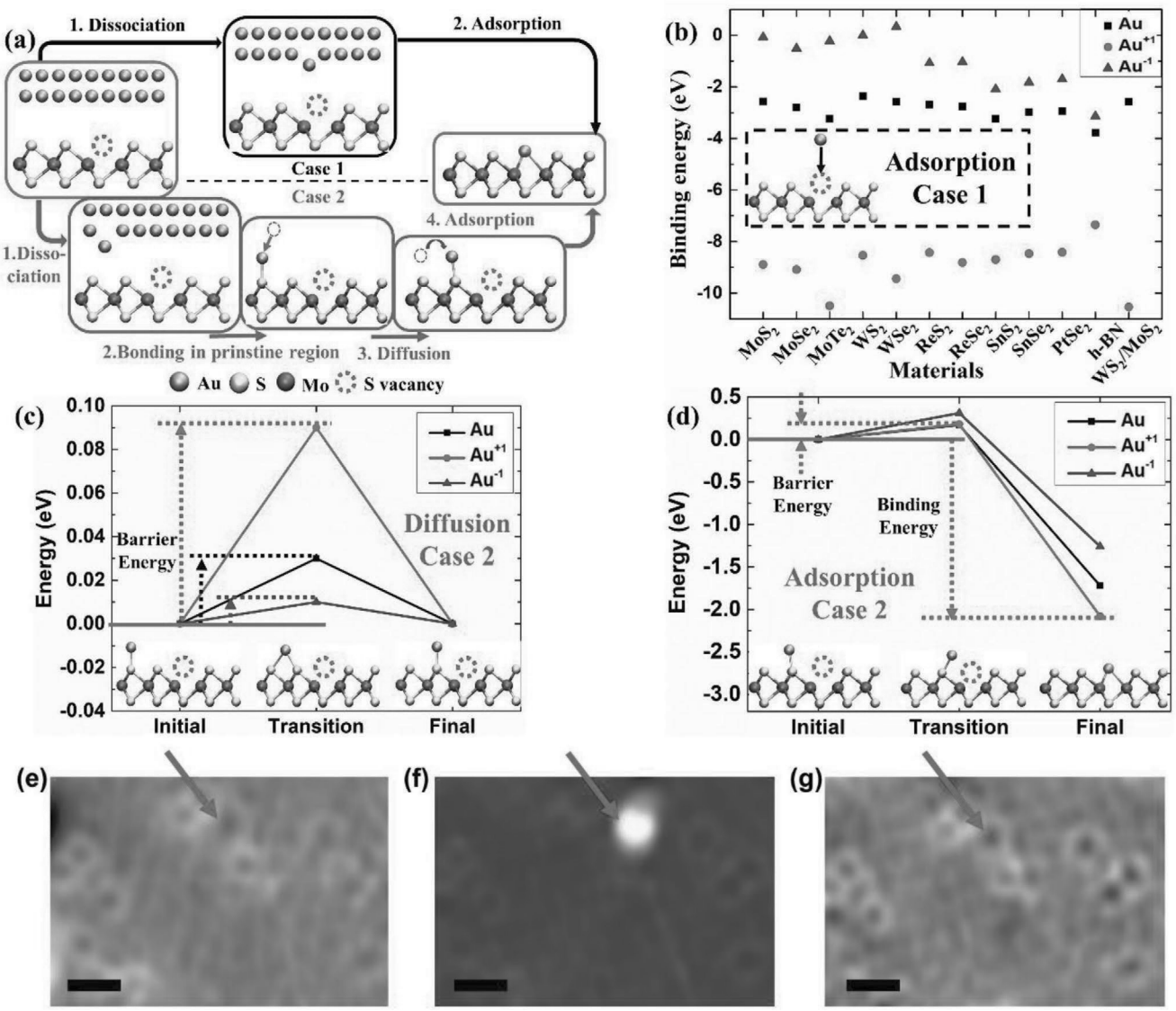

Figure 4. Calculated energy results and STM observations for dissociation–diffusion–adsorption (DDA) model. a) The schematics of different states in the DDA model. Case 1 (direct adsorption of Au in a vacancy) and Case 2 (Au first bonding to pristine region followed by diffusion across the surface for adsorption into a vacancy) are presented in black at the top and in blue at the bottom, respectively. b) The adsorption (or binding) energy of Au on a vacancy site for a dozen different 2D materials (Case 1). Inset: the schematic for adsorption step in Case 1 initially with isolated Au in a vacuum state. The energy difference between initial state and final state is the binding energy. c) Calculated diffusion pathway and barrier energy of the Au atom/ion from the top of one S atom to the top of a neighboring S atom in the pristine region of the MoS_2 surface (Case 2). The barrier energy is the amount of energy that must be added to go from the energy level of the initial state to that of the transition state as shown by black, red, and blue arrows for Au, Au^{+1}, and Au^{-1}, respectively. The considerably low energy barriers for Au diffusion across the pristine surface indicates that Au can easily move around. d) Calculated adsorption pathway and barrier and binding energies of an Au atom/ion from the top of one S atom in the pristine region to the S vacancy site on the MoS_2 surface (Case 2). The barrier energy and binding energy for Au^{+1} are indicated by red arrows. The relatively low barrier energy and large negative adsorption energy for Au/Au^{+1} indicates that both of them are favorable candidates for switching from both the kinetic and energetic viewpoints. Mo, S, and Au are shown in the color of magenta, yellow, and orange, respectively. The S vacancy on the surface is highlighted by the red dashed circle. e) STM image of monolayer MoS_2 surface with multiple V_S defects. A gold STM tip is placed on a defect location (marked with the arrow) and employed as a top electrode for an emulated device operation. f) An electric field (tip positive) causes dislocation of a gold atom from the STM tip. The gold atom (marked with the arrow) is absorbed at the V_S defect site and stably remains in this site during a subsequent STM imaging. g) STM image of the same area after the gold atom is removed from the defect site (marked with the arrow) with a device emulation under a reversed electric field. In addition to the removal of the gold atom, some V_S defects also diffuse during set-reset events. Scale bars:1 nm.

any defect site. The detailed barrier energy values of the diffusion step are presented in Table S4, Supporting Information. According to our first-principle calculations, the energy barrier for the Au atom/ion hopping from one S atom site to another is notably low (<0.1 eV), suggesting that Au atom/ion can easily move around the pristine region at room temperature. This is reasonable since the adsorption of Au atom/ion in the pristine region is weak, which makes them very mobile on the surface.

Regarding the concluding "adsorption" step in Case 2, Au will eventually diffuse to the atom close to the defect site, and subsequently bind to it, since Au can easily move around the surface. Figure 4d and Table S5, Supporting Information, present the calculated energies for transition and final states during the adsorption step. The low energy barrier (≤0.18 eV) suggests that Au/Au^{+1} is able to adsorb from the pristine region to the vacancy site, especially at elevated temperatures due to the thermal heating from the increased electrical current. Furthermore, this process releases a significant amount of energy (≥1.72 eV). The low energy barrier and large amount of energy released indicate that the adsorption of Au/Au^{+1} from the pristine region to the vacancy site is favorable both kinetically and energetically. On the other hand, the reversed process, that is, the Au/Au^{+1} departing the vacancy site to the pristine region, has a much higher energy barrier (1.89 eV). This suggests that it is much more difficult for Au/Au^{+1} to desorb from the vacancy site. Therefore, Au/Au^{+1} can stably bind to the vacancy site, acting as a conducting channel for LRS. In the RESET process, a high current passes through the conductive point or channel, providing adequate energy to overcome the barrier and driving Au/Au^{+1} away from the defect site. In contrast, the Au^{-1} ion has the highest energy barrier and the smallest binding energy. Thus, the Au^{-1} ion is the least favorable option to participate in the memory switching from both the kinetic and energetic viewpoints and is not likely to play an important role in resistive switching for the two scenarios discussed.

To experimentally support the dissociation–diffusion–adsorption model discussed above, we used a scanning tunneling microscope fitted with a gold tip. Scanning tunneling microscopy (STM) was initially used for atomic resolution imaging of the MoS_2 surface to locate and identify the sulfur vacancy defects (Figure 4e). Imaging was followed by a controlled physical contact of the gold STM tip with the MoS_2 surface and voltage sweeps to emulate a two-terminal vertical memory device operation. The STM image of the same location after a SET event shows a bright protrusion on the surface (Figure 4f). Stability of new defect under STM imaging shows that protrusion is not a diffusing atom. Instead, it is strongly bonded to surface and identified as a gold atom absorption at sulfur vacancy site.[41] A voltage sweep with opposite polarization can trigger a RESET event in which the gold atom is removed from the defect site (Figure 4g). The differences in sharpness and contrast of the STM images before and after the set-reset sequence show that the tip apex has been modified owing to the dissociation of a gold atom from the STM tip. As an extensive STM measurement, we not only landed the STM tip on top of the sulfur vacancy, but also in a defect-free region. As shown in Figure S5, Supporting Information, compared to the *I–V* curves which resemble resistive switching events observed at the defect locations, electrical measurements on defect-free regions reveal a tunneling-like *I–V* behavior with no switching phenomenon, supporting the essential role of defects (e.g., S vacancy) in a switching event.[41] To further elucidate the electronic nature of the defect before and after the switching event, the local density of states (LDOS) calculations (Figure S6, Supporting Information) show finite electronic states around the Fermi level after gold substitution in sulfur vacancy, indicating a metallic-like behavior near these gold absorption sites, which were initially insulating.

DDA model and related DFT calculations have a couple of imperfections. First, DFT calculation for benchmarking analysis is challenging. A number of variables, for example, defect density, defect category, Au states, electrical field, can be changed over a large range, making accurate prediction of NVRS in different materials computationally very expensive. But some insight can be learned from calculation results, for example, if a region contains very few defects, it is difficult for Au to find a defect site and stably bond to it (adsorption), and thus the adsorption may become the rate-limiting step. While for a defective region, adsorption becomes easy and other steps may take over the dominant role. Furthermore, although DDA model is established for monolayer resistive switching behavior from both theoretical and experimental perspectives, the physical mechanism for few-layer films is still not clear. Our hypothesis is based on conductive path through weak point(s)/region(s) in the thin film (e.g., grain boundary).[19] New methods and investigations are needed to fully understand the intriguing underlying physics in multilayer 2D-based devices.

In summary, we report non-volatile resistive switching behavior in various monolayer and few-layer 2D materials in TMDs, heterostructure and h-BN, alluding to a universal effect in 2D atomic sheets. A dissociation–diffusion–adsorption model is proposed, and detailed DFT calculations and STM observations are provided to support the model, which reveal that metal atom/ion adsorption into an individual vacancy can serve as a conductive point for NVRS. This is in contrast to transitional metal oxides where an extended conductive filament is required. The library of atomically thin 2D materials featuring non-volatile resistive switching can provide a promising platform for exploring the sub-nanometer scaling limit for emerging device concepts in non-volatile memory and neuromorphic computing. Our results motivate further research in defect and interface engineering, and the energetics and applications of defects in 2D materials.

Experimental Section

Material Source: A few 2D thin films were purchased from various companies, including MoS_2, ReS_2, and $ReSe_2$ from Sixcarbon Technology. SnS_2 and $SnSe_2$ were obtained from 2D Semiconductors. Other materials were provided by the authors' collaborators and details about the growth recipe can be found in previous publications.[22–25,42] Monolayer $MoSe_2$, WS_2, WSe_2 samples were prepared at 500 °C for 24 h by wafer-scale MOCVD.[23] $PtSe_2$ layers (≈3 nm) were grown by the direct selenization of Pt seeds (0.5 nm) in a CVD furnace on Au thin film.[24] As for heterostructure MoS_2/WS_2 film on Au foil, after finishing the CVD growth of monolayer WS_2, the WS_2/Au sample was then transferred to another furnace for subsequent MoS_2 CVD growth.[22] h-BN was synthesized by CVD on Ni foil using ammonia borane powder as precursor.[25] $MoTe_2$ flakes (HQ Graphene) were exfoliated onto a (285 nm) SiO_2/Si substrate using standard scotch tape technique.

Device Fabrication: Most materials were investigated using the crossbar device structure. For crossbar devices, BE were patterned by e-beam lithography and then deposited by e-beam evaporator (Cr 2 nm/Au 80 nm). Then 2D thin films were transferred on BE using either poly(dimethylsiloxane) (PDMS) stamp transfer[43] (used for MoS_2, WS_2, $MoSe_2$, WSe_2, ReS_2, $ReSe_2$, SnS_2, $MoTe_2$) or poly (methylmethacrylate) (PMMA) etching transfer[44] (used for h-BN and $SnSe_2$). For determining the appropriate transfer method for different 2D materials, the key consideration was based on the hydrophilic nature of the growth substrate. This was

because hydrophilic substrate was a prerequisite for PDMS transfer. In a PDMS stamp transfer process, 2D materials were in conformal contact with PDMS and then the whole system PDMS/2D layer was soaked in deionized water for about 30 min. Some growth substrates used in the study are hydrophilic, for example, SiO_2 and mica. For those substrates, water could diffuse into the interface between the growth substrate and 2D material with the subsequent release of the latter in what was known as water-assisted transfer. The PDMS/2D material stamp was aligned on to BE and then heated the whole system up to 90 degree for lifting PDMS and leaving 2D materials on substrate. For h-BN on Ni foil and $SnSe_2$ on sapphire, PMMA etching transfer was preferred. An ≈200 nm thick layer of supporting polymer PMMA was spin-coated and baked on a hotplate at 150 °C for 5 min. The PMMA/h-BN/Ni (or PMMA/$SnSn_2$/sapphire) stack was then immersed into etchant $(NH_4)_2S_2O_8$ (or NaOH) to etch the growth substrate. After triple-rinsing with deionized water, the sheet can be transferred onto the final substrate with prefabricated BE. After the transfer, the sample was left to dry out for 12 h at room temperature, followed by annealing at 150 °C for 10 min. The devices were then left for 24 h in acetone to remove the protective PMMA layer. All transferred samples were annealed in ultrahigh vacuum (UHV) at 300 °C for 2 h to remove any possible polymer residue. After transfer, TE were patterned and deposited using the same process as BE.

Compared to the crossbar device, which requires transfer and lithography, two materials—heterostructure (MoS_2/WS_2) and $PtSe_2$, were prepared using litho-free and transfer-free process, because they are grown on conductive substrate (Au) that could be directly employed as a global BE. And thus, no transfer was needed and TE were deposited through a shadow mask without any lithography. Figure S7a,b, Supporting Information, presents the schematic and optical image of litho-free and transfer-free device. Compared with crossbar devices, transfer-free devices had exactly the same stacking—Au/2D material/Au, but was realized using a simpler process with lower risk of polymer contamination at the expense of a relatively larger device area (>100 um^2). The *I*–*V* switching curves based on MoS_2 using litho-free and transfer-free device, and crossbar device are shown in Figure S7c, Supporting Information, and Figure 3, respectively. The favorable comparison of the same material with different device structures indicated that the switching phenomenon was intrinsic regardless of differences in process flow.

Characterization: The DC characteristics of the devices were taken on a Cascade probe station with an Agilent 4156 semiconductor parameter analyzer under ambient conditions. Raman and photoluminescence were performed on a Renishaw in-Via system using a 532 nm laser source.

STM measurements were carried on monolayer MoS_2 flakes mechanically exfoliated on a gold film. Samples were annealed up to 400 °C to increase sulfur vacancy density. STM imaging and device emulation experiments were performed with gold STM tips. To ensure a stable mechanical and electrical contact during the device emulations, the gold STM tip was first fixed on the surface using a stabilization voltage within the bandgap of MoS_2 than the tip was further approached to the surface for 2–4 Å.

Theoretical Calculations: Plane-wave density functional theory (DFT) software VASP[45] was utilized for first-principle calculations. The projector-augmented-wave (PAW) pseudopotentials were used for electron–ion interactions, and the generalized gradient approximation (GGA) in the flavor of the Perdew–Burke–Ernzerhof (PBE) functional[46] was adopted for the exchange-correlation interactions. For various 2D monolayer materials, including MoS_2, $MoSe_2$, $MoTe_2$, WS_2, WSe_2, ReS_2, $ReSe_2$, SnS_2, $SnSe_2$, $PtSe_2$, and BN, they were modeled by a periodic slab geometry with a vacuum separation of 21 Å in the out-of-plane direction. Similar setting was used to simulate the vertical heterostructure WS_2/MoS_2. Monolayer 2D materials were used because the Au interaction with the surface and defect site is only localized on the top layer. For the unit cell, all atoms were relaxed until the residual forces were below 0.01 eV $Å^{-1}$ and in-plane lattice constants were also optimized using the option of ISIF = 4 with the cutoff energy set at 400 eV. Different 2D materials had different lattice constants, and therefore different *k*-point samplings were used accordingly: 24 × 24 × 1 for MoS_2, $MoSe_2$, $MoTe_2$, WS_2, WSe_2, SnS_2, $SnSe_2$, $PtSe_2$, and WS_2/MoS_2; 12 × 12 × 1 for ReS_2 and $ReSe_2$; 30 × 30 × 1 for BN. Based on the optimized unit cell, a supercell structure was subsequently built to model the interaction between the surface and Au. The supercell size was also different depending on the 2D material's unit cell size: 5 × 5 × 1 supercell for MoS_2, $MoSe_2$, $MoTe_2$, WS_2, WSe_2, SnS_2, $SnSe_2$, $PtSe_2$, and WS_2/MoS_2; 3 × 3 × 1 supercell for ReS_2 and $ReSe_2$; 7 × 7 × 1 supercell for BN. To simulate the interaction between the Au and a vacancy on the 2D material surface, a chalcogenide atom (S, Se, or Te) was removed from the TMDs supercell structure, while a boron atom was removed from the BN supercell structure. For all supercell systems, the *k*-point sampling was chosen as 4 × 4 × 1, and all atoms were relaxed until the residual forces were below 0.01 eV $Å^{-1}$. Finally, to calculate barrier energies for Au diffusion on the surface and around the vacancy site, the nudged elastic band (NEB) method was used. Four intermediate images along the reaction path were created for the NEB optimization (force criterion is 0.05 eV $Å^{-1}$) to find the transition state and the barrier energy.

Supporting Information

Supporting Information is available from the Wiley Online Library or from the author.

Acknowledgements

The authors thank Dr. Hanglin Ye for schematics rendering in Figure 4. The authors thank Dr. An-Ping Li and Dr. Wonhee Ko for their help with STM measurements. This work was supported in part by the National Science Foundation (NSF) grant #1809017. The authors acknowledge use of Texas Nanofabrication Facilities supported by the NSF NNCI award #1542159. D.A. acknowledges the Presidential Early Career Award for Scientists and Engineers (PECASE) through the Army Research Office (W911NF-16-1-0277). Portion of this research (STM and theoretical calculations) used resources at the Center for Nanophase Materials Sciences, which is a U.S. Department of Energy Office of Science User Facility. L.L. acknowledges computational resources of the Compute and Data Environment for Science (CADES) at the Oak Ridge National Laboratory, which is supported by the Office of Science of the U.S. Department of Energy under Contract No. DE-AC05-00OR22725. Y.J. acknowledges supports from the Korea Institute of Energy Technology Evaluation and Planning (KETEP) and the Ministry of Trade, Industry and Energy (MOTIE) of the Republic of Korea (No. 20173010013340) and the VPR Advancement of Early Career Researchers award from the University of Central Florida. Y.Z. and J.S. acknowledge the financial support from the National Key Research and Development Program of China (2018YFA0703700) and National Natural Science Foundation of China (51925201).

Conflict of Interest

The authors declare no conflict of interest.

Author Contributions

R.G., X.W., and L.L. contributed equally to this work. R.G. carried out CVD growth of MoS_2, materials transfer and characterization, and device fabrication. X.W. performed electrical characterizations. L.L. conducted theoretical calculations. S.M.H. conducted STM measurements. Y.G. prepared $MoTe_2$-based memristor and related characterization. E.O., J.S., and H.C. performed CVD growth of $PtSe_2$, WS_2/MoS_2 heterostructure and h-BN, respectively. R.G., X.W., and D.A. analyzed the electrical data. All authors contributed to the article based on the draft prepared by R.G., X.W., and D.A. S.B., Y.Z., Y.J., J.L., and D.A. coordinated and supervised the project.

Keywords

2D materials, atomristors, memristors, resistive switching

Received: November 16, 2020
Published online: December 28, 2020

[1] G. R. Bhimanapati, Z. Lin, V. Meunier, Y. Jung, J. Cha, S. Das, D. Xiao, Y. Son, M. S. Strano, V. R. Cooper, L. Liang, S. G. Louie, E. Ringe, W. Zhou, S. S. Kim, R. R. Naik, B. G. Sumpter, H. Terrones, F. Xia, Y. Wang, J. Zhu, D. Akinwande, N. Alem, J. A. Schuller, R. E. Schaak, M. Terrones, J. A. Robinson, *ACS Nano* **2015**, *9*, 11509.
[2] D. Akinwande, C. J. Brennan, J. S. Bunch, P. Egberts, J. R. Felts, H. Gao, R. Huang, J.-S. Kim, T. Li, Y. Li, K. M. Liechti, N. Lu, H. S. Park, E. J. Reed, P. Wang, B. I. Yakobson, T. Zhang, Y.-W. Zhang, Y. Zhou, Y. Zhu, *Extreme Mech. Lett.* **2017**, *13*, 42.
[3] W. Choi, N. Choudhary, G. H. Han, J. Park, D. Akinwande, Y. H. Lee, *Mater. Today* **2017**, *20*, 116.
[4] N. Mounet, M. Gibertini, P. Schwaller, D. Campi, A. Merkys, A. Marrazzo, T. Sohier, I. E. Castelli, A. Cepellotti, G. Pizzi, N. Marzari, *Nat. Nanotechnol.* **2018**, *13*, 246.
[5] H. P. Wong, H. Lee, S. Yu, Y. Chen, Y. Wu, P. Chen, B. Lee, F. T. Chen, M. Tsai, *Proc. IEEE* **2012**, *100*, 1951.
[6] R. Ge, X. Wu, M. Kim, J. Shi, S. Sonde, L. Tao, Y. Zhang, J. C. Lee, D. Akinwande, *Nano Lett.* **2018**, *18*, 434.
[7] C. Tan, Z. Liu, W. Huang, H. Zhang, *Chem. Soc. Rev.* **2015**, *44*, 2615.
[8] A. A. Bessonov, M. N. Kirikova, D. I. Petukhov, M. Allen, T. Ryhänen, M. J. A. Bailey, *Nat. Mater.* **2015**, *14*, 199.
[9] D. Son, S. I. Chae, M. Kim, M. K. Choi, J. Yang, K. Park, V. S. Kale, J. H. Koo, C. Choi, M. Lee, J. H. Kim, T. Hyeon, D.-H. Kim, *Adv. Mater.* **2016**, *28*, 9326.
[10] C. Hao, F. Wen, J. Xiang, S. Yuan, B. Yang, L. Li, W. Wang, Z. Zeng, L. Wang, Z. Liu, Y. Tian, *Adv. Funct. Mater.* **2016**, *26*, 2016.
[11] V. K. Sangwan, D. Jariwala, I. S. Kim, K.-S. Chen, T. J. Marks, L. J. Lauhon, M. C. Hersam, *Nat. Nanotechnol.* **2015**, *10*, 403.
[12] L. Zhao, Z. Jiang, H.-Y Chen, J. Sohn, K. Okabe, B. Magyari-Köpe, H.-S. P. Wong, Y. Nishi, in *2014 IEEE Int. Electron Devices Meeting*, IEEE, Piscataway, NJ, USA **2014**, pp. http://doi.org/10.1109/IEDM.2014.7046998.
[13] Y. Shi, X. Liang, B. Yuan, V. Chen, H. Li, F. Hui, Z. Yu, F. Yuan, E. Pop, H. S. P. Wong, M. Lanza, *Nat. Electron.* **2018**, *1*, 458.
[14] H. Zhao, Z. Dong, H. Tian, D. DiMarzi, M.-G. Han, L. Zhang, X. Yan, F. Liu, L. Shen, S.-J. Han, S. Cronin, W. Wu, J. Tice, J. Guo, H. Wang, *Adv. Mater.* **2017**, *29*, 1703232.
[15] X. Wu, R. Ge, P.-A. Chen, H. Chou, Z. Zhang, Y. Zhang, S. Banerjee, M.-H. Chiang, J. C. Lee, D. Akinwande, *Adv. Mater.* **2019**, *31*, 1806790.
[16] R. Ge, X. Wu, M. Kim, P. Chen, J. Shi, J. Choi, X. Li, Y. Zhang, M. Chiang, J. C. Lee, D. Akinwande, in *2018 IEEE Int. Electron Devices Meeting (IEDM)*, IEEE, Piscataway, NJ, USA **2018**, https://doi.org/10.1109/IEDM.2018.8614602.
[17] M. Kim, R. Ge, X. Wu, X. Lan, J. Tice, J. C. Lee, D. Akinwande, *Nat. Commun.* **2018**, *9*, 2524.
[18] M. Kim, E. Pallecchi, R. Ge, X. Wu, G. Ducournau, J. C. Lee, H. Happy, D. Akinwande, *Nat. Electron.* **2020**, *3*, 479.
[19] R. Xu, H. Jang, M.-H. Lee, D. Amanov, Y. Cho, H. Kim, S. Park, H.-j. Shin, D. Ham, *Nano Lett.* **2019**, *19*, 2411.
[20] Y. Liu, N. O. Weiss, X. Duan, H.-C. Cheng, Y. Huang, X. Duan, *Nat. Rev. Mater.* **2016**, *1*, 16042.
[21] M. Lanza, H. S. P. Wong, E. Pop, D. Ielmini, D. Strukov, B. C. Regan, L. Larcher, M. A. Villena, J. J. Yang, L. Goux, A. Belmonte, Y. Yang, F. M. Puglisi, J. Kang, B. Magyari-Köpe, E. Yalon, A. Kenyon, M. Buckwell, A. Mehonic, A. Shluger, H. Li, T.-H. Hou, B. Hudec, D. Akinwande, R. Ge, S. Ambrogio, J. B. Roldan, E. Miranda, J. Suñe, K. L. Pey, et al., *Adv. Electron. Mater.* **2019**, *5*, 1800143.
[22] J. Shi, R. Tong, X. Zhou, Y. Gong, Z. Zhang, Q. Ji, Y. Zhang, Q. Fang, L. Gu, X. Wang, Z. Liu, Y. Zhang, *Adv. Mater.* **2016**, *28*, 10664.
[23] K. Kang, S. Xie, L. Huang, Y. Han, P. Y. Huang, K. F. Mak, C.-J. Kim, D. Muller, J. Park, *Nature* **2015**, *520*, 656.
[24] S. S. Han, J. H. Kim, C. Noh, J. H. Kim, E. Ji, J. Kwon, S. M. Yu, T.-J. Ko, E. Okogbue, K. H. Oh, H.-S. Chung, Y. Jung, G.-H. Lee, Y. Jung, *ACS Appl. Mater. Interfaces* **2019**, *11*, 13598.
[25] A. Ismach, H. Chou, D. A. Ferrer, Y. Wu, S. McDonnell, H. C. Floresca, A. Covacevich, C. Pope, R. Piner, M. J. Kim, R. M. Wallace, L. Colombo, R. S. Ruoff, *ACS Nano* **2012**, *6*, 6378.
[26] S. Xiao, P. Xiao, X. Zhang, D. Yan, X. Gu, F. Qin, Z. Ni, Z. J. Han, K. Ostrikov, *Sci. Rep.* **2016**, *6*, 19945.
[27] M. Yamamoto, S. T. Wang, M. Ni, Y.-F. Lin, S.-L. Li, S. Aikawa, W.-B. Jian, K. Ueno, K. Wakabayashi, K. Tsukagoshi, *ACS Nano* **2014**, *8*, 3895.
[28] Q. Song, H. Wang, X. Pan, X. Xu, Y. Wang, Y. Li, F. Song, X. Wan, Y. Ye, L. Dai, *Sci. Rep.* **2017**, *7*, 1758.
[29] D. Chenet, O. B. Aslan, P. Huang, C. Fan, A. Zande, T. Heinz, J. Hone, *Nano Lett.* **2015**, *15*, 5667.
[30] N. R. Pradhan, C. Garcia, B. Isenberg, D. Rhodes, S. Feng, S. Memaran, Y. Xin, A. McCreary, A. R. H. Walker, A. Raeliarijaona, H. Terrones, M. Terrones, S. McGill, L. Balicas, *Sci. Rep.* **2018**, *8*, 12745.
[31] P. Chen, J. Shang, Y. Yang, R. Wang, X. Cheng, *Appl. Surf. Sci.* **2017**, *419*, 460.
[32] L. Kong, X. Zhang, Q. Tao, M. Zhang, W. Dang, Z. Li, L. Feng, L. Liao, X. Duan, Y. Liu, *Nat. Commun.* **2020**, *11*, 1866.
[33] A. Chen, M. Lin, in *2011 International Reliability Physics Symp.*, IEEE, Piscataway, NJ, USA, https://doi.org/10.1109/IRPS.2011.5784590.
[34] Y.-F. Kao, W. C. Zhuang, C.-J. Lin, Y.-C. King, *Nanoscale Res. Lett.* **2018**, *13*, 213.
[35] D. Wang, Y. Dai, J. Xu, L. Chen, Q. Sun, P. Zhou, P. Wang, S. Ding, D. W. Zhang, *IEEE Electron Device Lett.* **2016**, *37*, 878.
[36] M. Wang, S. Cai, C. Pan, C. Wang, X. Lian, Y. Zhuo, K. Xu, T. Cao, X. Pan, B. Wang, S.-J. Liang, J. J. Yang, P. Wang, F. Miao, *Nat. Electron.* **2018**, *1*, 130.
[37] K. Hilpert, K. A. Gingerich, *Ber. Bunsenges. Phys. Chem.* **1980**, *84*, 739.
[38] C.-N. Peng, T.-C. Chan, W.-Y. Chang, Y.-C. Wang, H.-W. Tsai, W.-W. Wu, L.-J. Chen, Y.-L. Chueh, *Nanoscale Res. Lett.* **2012**, *7*, 559.
[39] M. Pandey, F. A. Rasmussen, K. Kuhar, T. Olsen, K. W. Jacobsen, K. S. Thygesen, *Nano Lett.* **2016**, *16*, 2234.
[40] B. Huang, H. Lee, *Phys. Rev. B* **2012**, *86*, 245406.
[41] S. M. Hus, R. Ge, P.-A. Chen, L. Liang, G. E. Donnelly, W. Ko, F. Huang, M.-H. Chiang, A.-P. Li, D. Akinwande, *Nat. Nanotechnol.*, https://doi.org/10.1038/s41565-020-00789-w.
[42] A. Ismach, H. Chou, P. Mende, A. Dolocan, R. Addou, S. Aloni, R. Wallace, R. Feenstra, R. S. Ruoff, L. Colombo, *2D Mater.* **2017**, *4*, 025117.
[43] X. Ma, Q. Liu, D. Xu, Y. Zhu, S. Kim, Y. Cui, L. Zhong, M. Liu, *Nano Lett.* **2017**, *17*, 6961.
[44] G. B. Barin, Y. Song, I. de Fátima Gimenez, A. G. Souza Filho, L. S. Barreto, J. Kong, *Carbon* **2015**, *84*, 82.
[45] G. Kresse, J. Furthmüller, *Comput. Mater. Sci.* **1996**, *6*, 15.
[46] J. P. Perdew, K. Burke, M. Ernzerhof, *Phys. Rev. Lett.* **1996**, *77*, 3865.